Journal of Materials Chemistry C

PAPER

View Article Online
View Journal | View Issue

Cite this: J. Mater. Chem. C, 2017, 5, 10761

K_2MnF_6 as a precursor for saturated red fluoride phosphors: the struggle for structural stability

Reinert Verstraete, [ab] Heleen F. Sijbom, [ab] Katleen Korthout,[ab] Dirk Poelman, [ab] Christophe Detavernier[c] and Philippe F. Smet *[ab]

Phosphor-converted white light-emitting diodes (LEDs) are currently taking over the lighting market because of their high luminous efficiency, environmentally friendly nature and long lifetime. A new generation of saturated red fluoride phosphors, using Mn^{4+} as the activator, has gained interest in further enhancing the color rendering properties and efficiency of white LEDs for lighting and display applications. They can be described as $A_2MF_6:Mn^{4+}$ (A = K, Na, Sc, NH_4 and M = Si, Ge, Ti, Sn), $KNaMF_6:Mn^{4+}$, $BaMF_6:Mn^{4+}$ (M = Si, Ti) or $ZnMF_6{\cdot}H_2O$ (M = Si, Ge) compounds, in which Mn is a substitute for the M(IV) element of the fluoride host. A two-step co-precipitation synthesis method has recently been developed because of the increased control of the Mn valence state and the relatively low cost. In this method, K_2MnF_6 is first synthesized as a precursor which then serves as a source for the preparation of $[MnF_6]^{2-}$ complexes in further phosphor synthesis. In-house production of K_2MnF_6 is required as it quickly degrades. Here, we investigate the structural properties after synthesis, as well as the main degradation routes of K_2MnF_6 when the material is subjected to heat and humidity or used in further synthesis reactions. It is found that impurities, such as KHF_2, $K_2MnF_5{\cdot}H_2O$ and Mn ions in an oxygen coordination, can be formed as a result of parasitic reactions during synthesis. Even in pure K_2MnF_6, degradation occurs due to heat and hydrolysis both of which induce reduction of the Mn^{4+} ion. Heating in air causes the material to form Mn^{2+} as $KMnF_3/KF{\cdot}MnF_2$ starts to form at high temperatures due to hydrolysis. In dilute HF solutions the Mn^{4+} ion is partially reduced to Mn^{3+}, often incorporated in hydrated structures as $KMnF_4{\cdot}H_2O$ and $K_2MnF_5{\cdot}H_2O$. The Mn^{3+} ion is found to affect the optical absorption properties.

Received 4th July 2017,
Accepted 13th September 2017

DOI: 10.1039/c7tc02992f

rsc.li/materials-c

Introduction

Ever since the introduction of high-brightness blue light-emitting diodes (LEDs), much effort has been put into the development of white LEDs (wLEDs). Progress in the field of lighting has come to the point at which wLEDs are now taking over the market due to their improved stability and efficiency in comparison with more traditional light sources such as incandescent or fluorescent lamps.[1–3] wLEDs can be based on the combination of three separate LED chips which emit blue, green and red light, respectively. However most wLEDs make use of at least one photoluminescent material, a phosphor, hence the name phosphor-converted LEDs (pc-LEDs).[4] Here, the combined emission from the blue LED chip and the phosphors yields white light. $Y_3Al_5O_{12}:Ce^{3+}$ (YAG:Ce) is often used in single-phosphor pc-LEDs because of the high stability and efficiency of this phosphor.[2,5] However, without any additional phosphors, the obtained white light lacks in the green and red parts of the optical spectrum, hence leading to a high correlated color temperature (CCT) and a poor color rendering index (CRI) (CCT $>$ 6000 K, R_a $<$ 80).[6] Therefore, other phosphor materials are often used in a phosphor blend. By adding a red component, one can lower the color temperature of wLEDs yielding warm-white light. On the one hand, the red phosphor emission above 650 nm should be minimal, as the human eye sensitivity is very low in this wavelength region. On the other hand, especially for display applications, saturated red phosphors are preferred as these enlarge the color gamut of the display (*e.g.* BT. 2020 guidelines for UHD displays[7]). Suitable new red phosphor materials should therefore show a saturated red emission below 650 nm.[8] Apart from the optical requirements, the stability of red phosphor materials should also be adressed. Degradation of phosphor materials can lead to color changes or lumen losses over time when the material is stressed by heat (with temperatures up to 200 °C in high brightness LEDs[9]) or humidity from the environment. The study on the prevention of degradation becomes increasingly

[a] LumiLab, Department of Solid State Sciences, Ghent University, Ghent, Belgium. E-mail: Philippe.Smet@UGent.be
[b] Center for Nano- and Biophotonics (NB-Photonics), Ghent University, Ghent, Belgium
[c] Conformal Coating of Nanomaterials (CoCooN), Department of Solid State Sciences, Ghent University, Ghent, Belgium

more important as the lifetime of current LEDs is expected to be at least 50.000 hours. In the past, sulfides and especially nitrides, *e.g.* (Sr,Ca)S:Eu^{2+},[10] $CaAlSiN_3$:Eu^{2+},[11] and $(Sr,Ba)_2Si_5N_8$:Eu^{2+},[12] have been commercially used as red phosphor materials.

However, drawbacks such as poor thermal quenching and hydrolysis of the sulfides and a too broad emission band for many nitride phosphors, led to research towards a new generation of saturated red-emitting phosphors which do not involve rare-earth dopants.[8] These phosphors, using Mn^{4+} as an activator[13] in a fluoride host, are promising as they show saturated red emission below 650 nm and low thermal quenching at LED operating temperatures. K_2SiF_6:Mn^{4+}, with an emission peak around 630 nm, can be considered as a prototype material for Mn^{4+} fluorides.[14] Its synthesis and properties have been recently reviewed.[15] $BaSiF_6$:Mn^{4+},[16] $KNaSiF_6$:Mn^{4+},[17] K_2TiF_6:Mn^{4+},[18,19] Cs_2TiF_6:Mn^{4+},[20] K_2GeF_6:Mn^{4+},[21] Na_2GeF_6:Mn^{4+}[22] and $BaGeF_6$:Mn^{4+}[23] are just a few examples of fluoride phosphors with a similar emission spectrum which can be attributed to Mn^{4+} and its fluorine ligands. $BaMF_6$:Mn^{4+} (M = Si, Ge), $KNaMF_6$:M^{4+} and A_2MF_6:Mn^{4+} (A = K, Na, Sc, NH_4 and M = Si, Ge, Ti, Sn) red phosphors have Mn^{4+} surrounded by six fluorine atoms, creating $[MnF_6]^{2-}$ complexes with an octahedral shape. These complexes show a characteristic saturated red emission around 630 nm upon blue or UV excitation, which is ideal for LED applications. While solid state reactions are often used to produce conventional phosphors, wet chemical synthesis routes are used for fluoride phosphors. The main challenge during the synthesis proves to be the large variety of valence states that Mn can adopt, ranging from 0 to 7+. In the past, synthesis of fluoride phosphors has been performed using various methods including wet chemical etching,[17,21,22,24,25] redox precipitation[14,26] and co-crystallization (cation exchange).[19,27,28] Furthermore, hydrothermal methods[16,19,23] have also been proposed. More recently, an improved two-step co-precipitation method has gained strong interest because of the improved control of the Mn valence.[16,18,20,29] K_2MnF_6 is synthesized during the first synthesis step.[18,28,30–32] This precursor material then provides anionic $[MnF_6]^{2-}$ complexes, which can be incorporated into various fluoride host materials such as K_2TiF_6 or K_2SiF_6. Fluorine coordination of Mn stabilizes the 4+ valence state, preventing reduction towards lower valence states. Nevertheless, K_2MnF_6 is not commercially available due to its instability with respect to heat and moisture, requiring a delicate in-house synthesis. As defects and impurities in the final phosphors, caused by impure or degraded K_2MnF_6, can affect thermal quenching and phosphor efficiency,[9,33] a thorough understanding of the synthesis and degradation of K_2MnF_6 is in place. Here, we investigate the structural and optical properties of K_2MnF_6 after synthesis as well as the effect of heat, humidity and further phosphor synthesis steps.

Experimental

K_2MnF_6 powders were prepared using the method of Bode and Bandte.[32] Here, 36 g of KF and 2 g of $KMnO_4$ were dissolved in 150 ml of 40% HF, preserving a 1 : 49 – $KMnO_4$: KF ratio. The excess KF facilitates fluorine complexation of the Mn ions while the acidic synthesis environment limits hydroxide formation during synthesis. Reduction of manganese from Mn^{7+} to Mn^{4+} was performed by dropwise addition of 35% H_2O_2 with vigorous stirring. The addition rate of the reducing agent was controlled to prevent parasitic hydrolysis reactions, exclude excessive reduction of the Mn ions and control the formation of O_2. Adding H_2O_2 induces a colour change of the solution which turns from purple, over light purple towards dark and finally light brown. Furthermore, a yellow precipitate forms on the bottom of the reaction cup. Stopping the H_2O_2 addition at the right moment is crucial but rather challenging due to ongoing reactions even after the last addition of H_2O_2. However, one typically stops the addition as soon as the solution evolves to light brown. For the aforementioned synthesis conditions, addition of around 2 ml of H_2O_2 proved to yield the maximal amount of K_2MnF_6 while minimizing the amount of impurity phases. After decantation, filtration and a washing treatment with HF and acetone, the precipitate can be dried and a bright yellow K_2MnF_6 powder sample is obtained. The overall synthesis reaction can be described as:[31]

$$2KMnO_4 + 2KF + 10HF + 3H_2O_2 \rightarrow 2K_2MnF_6 + 8H_2O + 3O_2\uparrow$$

Structural properties were investigated by *in-* and *ex situ* X-ray diffraction (XRD) experiments. During *in situ* XRD measurements, a sample was placed on a heating stage in a reaction chamber filled with air or N_2 and subsequently heated at a rate of 0.2 °C s^{-1} from room temperature (RT) up to 600 °C. A Bruker Advance D8 diffractometer equipped with a linear X-ray detector was used for *in situ* XRD monitoring of the samples in a 2θ range of 30.6° to 49.6°. *Ex situ* measurements in air were performed using both a Bruker Advance D8 and a Bruker D5000 diffractometer. Cu $K\alpha_1$ tube emission was used in all XRD measurements. A Memmert HCP 108 weathering chamber was used to maintain ambient atmospheres with predefined heat and humidity levels in which samples could be aged over time. Optical diffuse reflectance measurements on the powders were performed using a Varian Cary 500 spectrometer, equipped with an internal 110 mm $BaSO_4$-coated integrating sphere. X-ray absorption spectroscopy (XAS) at the Mn K edge was performed at the European Synchrotron Radiation Facility (ESRF) in Grenoble, France, beam line BM26A.

Results and discussion

As previously mentioned, manganese can take on many valence states, the most common ones being 0, 2+, 3+, 4+ and 7+. This creates a challenge for the synthesis because Mn ions are sensitive to valence changes and in particular excessive reduction if the temperature and/or H_2O_2 addition rate are insufficiently controlled. Moreover, in the following, it will be shown that parasitic species often exist after the synthesis of K_2MnF_6, potentially contaminating further phosphor synthesis steps and affecting both structural and luminescence properties of the final phosphor. While some impurities can be eliminated

by a washing treatment, other impurities can remain present in K_2MnF_6, often without any trace in the X-ray diffraction pattern. Even when purified, care should be taken as any additional reaction step might cause K_2MnF_6, and hence the $[MnF_6]^{2-}$ complexes, to degrade.

Structural properties

K_2MnF_6 exhibits two crystalline phases: a low-temperature hexagonal phase and a high-temperature cubic phase. Both structures are displayed in Fig. 1. MnF_6 octahedrons are clearly visible in both phases. However, in the hexagonal phase, two distinct Mn sites are present which exhibit a different orientation of the $[MnF_6]^{2-}$ coordination complex. Half of the complexes are tilted around the *a*-axis. The complexes in the cubic phase only have one orientation making all Mn sites identical. Phase transition from the hexagonal to the cubic structure occurs around 440 °C in an inert N_2 atmosphere as can be seen in the *in situ* XRD pattern shown in the upper part of Fig. 2. Here, the XRD pattern within a 2θ range of 30.6° to 49.6° is shown as a function of increasing sample temperature, on going from RT up to 500 °C. Heating was performed under an inert N_2 atmosphere to prevent any moisture-induced degradation of K_2MnF_6. The RT *ex situ* XRD patterns of the pristine hexagonal and cubic phase after heating in N_2 are shown in Fig. 3. The final cubic structure could be maintained when the sample was cooled to room temperature. However, after storage of the powder in air for 17 days, the cubic phase almost completely returned to the hexagonal structure indicating that the cubic phase is not stable over time at room temperature.

Note that in Fig. 2, a large thermal shift towards considerable smaller values for 2θ is observed for all XRD peaks of the hexagonal K_2MnF_6 when the temperature is increased, indicating a rather large thermal expansion of the lattice. Since K_2MnF_6 is hexagonal below 400 °C, it can be expected that the positive thermal expansion of the lattice is anisotropic. The peak shifts can be related to the elongation of the lattice vectors *a*, *b* and *c* of the unit cell as the temperature is increased. Gaussian peak fitting of the (110) and (004) diffraction peaks at RT and 400 °C showed that the lattice has expanded in an anisotropic way with an estimated elongation of 2.1% along the *c*-axis, and only 1.6% along the *a* and *b* axes. Hence, anisotropic expansion might involve rotation of all

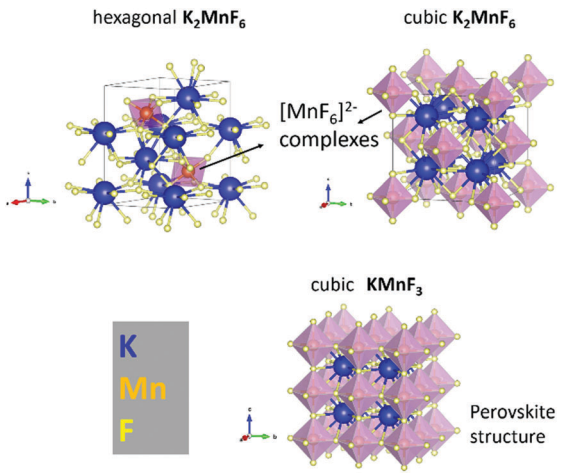

Fig. 1 Top: Unit cell of the hexagonal (low temperature) and cubic (high temperature) phase of K_2MnF_6. The purple semi-transparent octahedrons represent the $[MnF_6]^{2-}$ complexes. Bottom: Structure of $KMnF_3$ which tends to form during heating of K_2MnF_6.

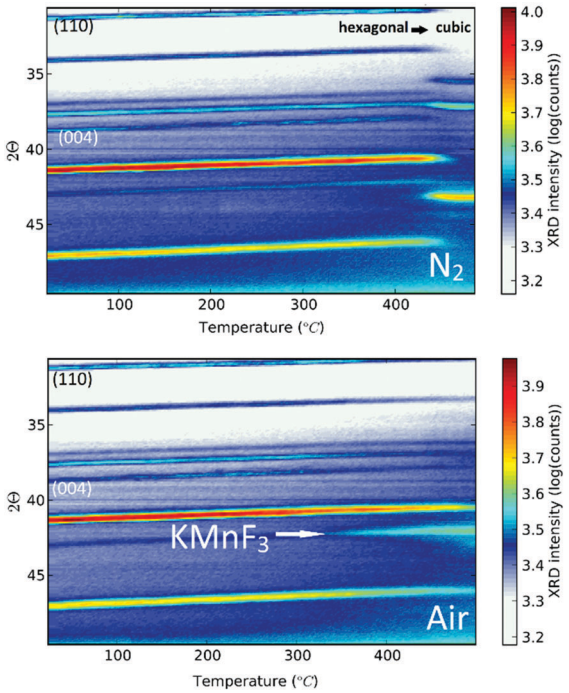

Fig. 2 *In situ* XRD spectrum of K_2MnF_6, heated from RT to 500 °C under a N_2 atmosphere (top) or in air (bottom). A phase transformation is visible around 440 °C when N_2 is used as an annealing atmosphere. No phase transformation is observed in air, but $KMnF_3$ is slowly formed with increasing temperatures.

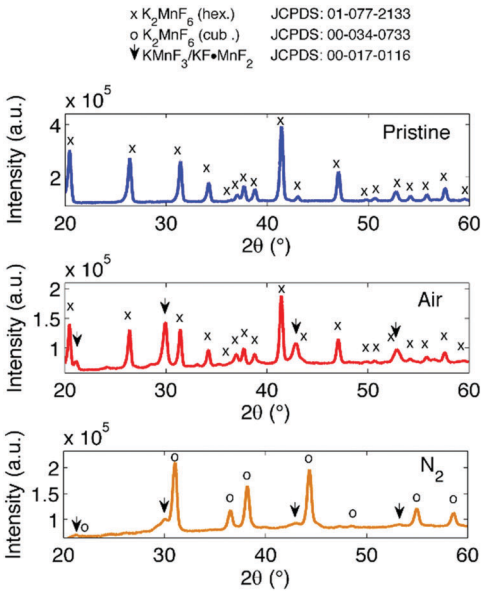

Fig. 3 *Ex situ* XRD spectrum of K_2MnF_6 before heating (top) and after heating in air or N_2 (middle and bottom, respectively).

$[MnF_6]^{2-}$ octahedral complexes to ultimately align with the *c*-axis. This positive thermal expansion is next followed by negative thermal expansion in the vicinity of phase transition (see the N_2 case in Fig. 2). Negative expansion could be caused by coupled rotation of rigid $[MnF_6]^{2-}$ units when the temperature is close to the transition temperature. Perovskite structures are known to exhibit so-called rigid unit modes (RUMs).[34,35] These are low-energy phonon modes in which the rigid units are rotationally coupled, often leading to contracting structures upon heating. Negative thermal expansion is an indicator for the existence of RUMs.

When, on the other hand, heating of K_2MnF_6 is performed in air instead of N_2, a different behaviour is found. The bottom figure of Fig. 2 shows broadening of the peak at $2\theta = 43^\circ$ instead of phase transition. Remarkably, the intensity of this peak increases above 300 °C while the other peaks tend to fade out above this temperature. This is explained by the formation of $KMnF_3$ ($KF{\cdot}MnF_2$) which also has a diffraction peak around $2\theta = 43^\circ$. The structure of $KMnF_3$ (lower part of Fig. 1) is similar to the cubic phase of K_2MnF_6, the difference being the doubled number of coordination complexes within a cubic unit cell, which are corner-sharing in the case of $KMnF_3$ as a result of the reduction of Mn^{4+} to Mn^{2+}. In this way, a perovskite structure appears. Although more pronounced in air, thermal degradation is still present to some degree when N_2 is used, as can be verified in Fig. 3. As will be clarified later on, increased thermal degradation in air is due to the hygroscopic nature of K_2MnF_6. Water vapour present in air can lead to hydrolysis of the $[MnF_6]^{2-}$ complexes which in turn facilitates the reduction of Mn^{4+} and hence the structural change. Probably, the formation of $KMnF_3$ is accompanied by the evaporation of HF as the fluorine content is lowered in $KMnF_3$ compared to K_2MnF_6. It is furthermore suspected that HF liberation can take place even at room temperature as a consequence of hydrolysis. This is evidenced by storing K_2MnF_6 in a glass vial under air. The vial gets eroded over time while the powder at the glass interface turns dark brown in a period of days up to weeks, probably depending on the purity of the K_2MnF_6 powder. We will elaborate on synthesis impurities in the next section. SEM-EDX measurements to investigate the brown discoloration showed the presence of Si and O as additional elements, indicating that they result from etching reactions at the glass interface. Nevertheless, the formed products could not be identified as a separate crystalline phase as the XRD pattern did not show any additional peaks next to K_2MnF_6.

Synthesis impurities

The excess KF that is used during synthesis ensures sufficient fluorination of Mn ions. Fluorination prevents excessive reduction towards Mn valences lower than 4+, which would be accompanied by the formation of oxygen containing or hydrated structures by interaction of Mn with H_2O and H_2O_2 in the synthesis solution as will be discussed later on. As can be seen in Fig. 4, the end result after synthesis can contain several impurities after precipitation and drying. The main impurity proves to be KHF_2, a corrosive salt that is often used as a glass etchant. The salt can result from the interaction of HF with KF in the synthesis solution:

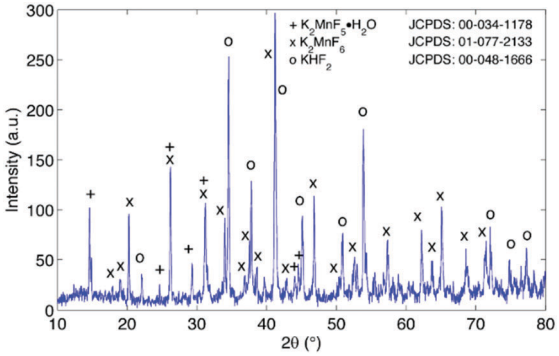

Fig. 4 *Ex situ* XRD pattern after K_2MnF_6 synthesis without washing treatment. KHF_2 and $K_2MnF_5{\cdot}H_2O$ formed during K_2MnF_6 synthesis as a result of KF–HF interaction and Mn–H_2O or Mn–H_2O_2 interaction, respectively.

$$HF + KF \rightarrow KHF_2 \text{ (synthesis solution)}$$

Purification requires an additional washing treatment with HF before drying, in this way removing any residual KHF_2. The importance of proper purification of K_2MnF_6 should not be underestimated. Not only is the KHF_2 impurity a hazardous corrosive compound on its own, but elevated temperatures also lead to the decomposition and melting of the phase which is accompanied by the evaporation of HF. The corrosive behaviour of this impurity could explain the observed corrosion of K_2MnF_6 powder stored in glass vials as was mentioned in the previous section. To investigate the effect of hydrolysis on samples containing K_2MnF_6 and KHF_2, two samples were heated in air from RT up to 600 °C, one of which was aged in a weathering chamber first (see Fig. 5).

The weathering conditions of the aged sample were 24 h at 85 °C/85% relative humidity (RH) followed by 48 h at 40 °C/40% RH. The XRD patterns of both samples before heat treatment can be found in Fig. 6, showing that the amount of KHF_2 impurity before heating was larger in the aged sample. Despite the resulting intensity differences in the *in situ* XRD patterns of Fig. 5, the global thermal behaviour of both samples can be considered as equal. When the powders are heated above 239 °C, the powders start to release HF because KHF_2 melts and decomposes into KF and HF at this temperature. Two relatively weak subsequent phase transitions occur after melting until crystalline $KMnF_3/KF{\cdot}MnF_2$, KF and MnF_2 are ultimately formed above 300 °C as can be verified in Fig. 5. A comparison of Fig. 5 with Fig. 2 indicates that even small amounts of KHF_2 can drastically lower the decomposition temperature of K_2MnF_6. Note that two additional XRD peaks are present in the aged sample which are identified as KF resulting from the larger amount of KHF_2 melt in the aged sample and hydrolysis of KHF_2 during aging. In Fig. 4, one can observe a second synthesis-related impurity next to KHF_2. As was shown by Kasa *et al.*,[36] uncontrolled reduction of Mn can lead to the formation of a pink precipitate. In some of the powders synthesized in this work, pink coloured

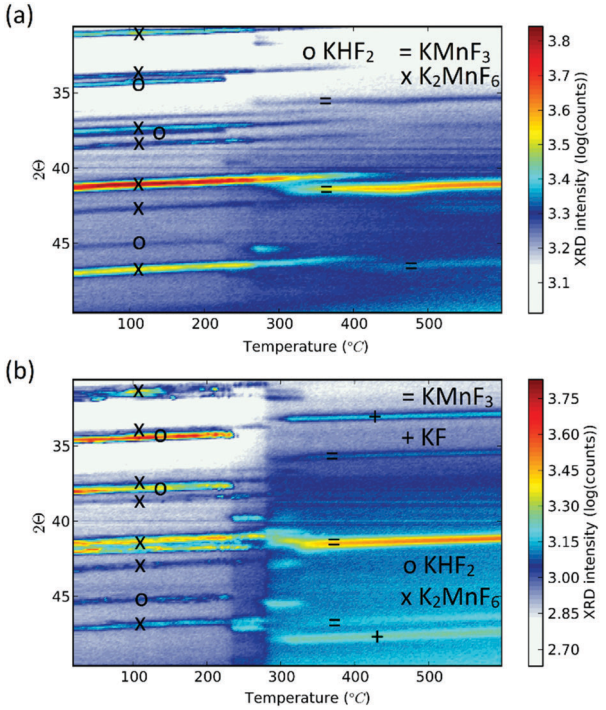

Fig. 5 *In situ* XRD measurements on impure powders which were (a) fresh and (b) aged. Both samples contain K_2MnF_6 and KHF_2 at room temperature as no washing step was performed during synthesis. KHF_2 melts at 239 °C, after which decomposition causes HF evaporation. At high temperatures $KMnF_3$ is formed. KF is additionally formed in (b) because the pristine amount of KHF_2 was higher (see Fig. 6) and hydrolysis of KHF_2 occurred during the ageing process.

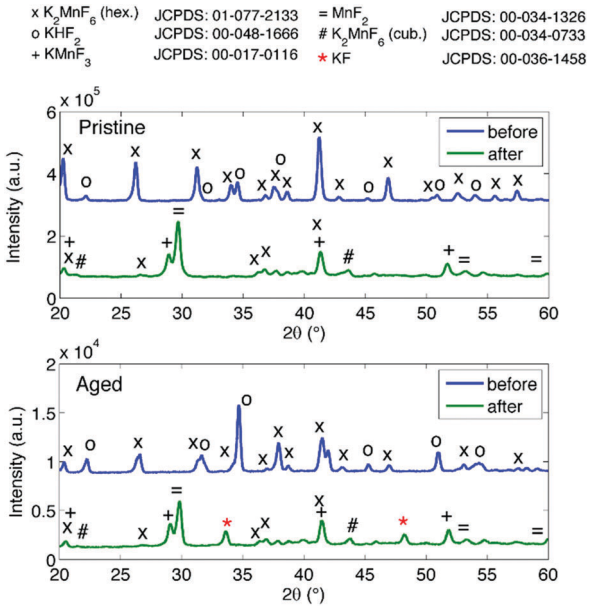

Fig. 6 *Ex situ* XRD measurements at RT on a pristine and aged impure powder before and after heating under an inert atmosphere. The same behaviour is present in both samples. Two additional peaks are seen in the aged sample, indicated by the red asterisks. These are due to KF formation because of the high pristine amount and hydrolysis of KHF_2 in this sample.

particles were occasionally formed next to the yellow K_2MnF_6 particles. The XRD analysis in Fig. 4 identified the pink phase as $K_2MnF_5{\cdot}H_2O$, in agreement with the work of Kasa *et al.*[36] The structure of $K_2MnF_5{\cdot}H_2O$ is shown in Fig. 7. Water molecules are incorporated in this crystalline structure; however the complexes are not attacked by the hydration process. Nevertheless, hydrate formation can impede further phosphor synthesis as Mn has been reduced to the 3+ valence state rather than the 4+ valence state.

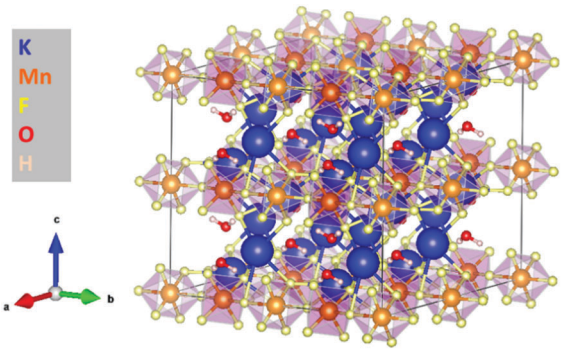

Fig. 7 Structure of the $K_2MnF_5{\cdot}H_2O$ hydrate formed during synthesis.

Further phosphor synthesis: degradation in HF solution

Up to this point, we discussed the risk of impurity phase formation as a result of KF–HF interaction, hydrolysis and hydration during synthesis. Moreover we discussed crystallization of $KMnF_3$ when K_2MnF_6 is heated in air. Equally important is the stability of Mn^{4+} when the purified K_2MnF_6 is used as a precursor in further synthesis steps of fluoride phosphors. Typically the precursor material will be dissolved in a KF/HF solution which is brought to elevated temperatures even up to 60 °C.[30] K_2MnF_6 dissociates into K^+ and $[MnF_6]^{2-}$, making the latter vulnerable to hydrolysis. To study these effects, a purified K_2MnF_6 sample was dissolved into a 40% HF solution which was subsequently heated in a water bath at set temperatures. A colour change of the solution could be observed: the pristine yellowish solution at 20 °C turned dark brown at 55 °C, with a gradual change in between. The colour change indicates that the $[MnF_6]^{2-}$ complexes were (at least partially) decomposed by the solution. To further investigate the effect of the solution temperature on the $[MnF_6]^{2-}$ complexes, acetone was added as a nonsolvent to form precipitates at different temperatures. Analysis with *ex situ* XRD on the dried precipitates was performed to identify the dominant species formed at each temperature. The resulting XRD spectra of the precipitates are shown in Fig. 8. Phase identification indicates that the K_2MnF_6 powder gradually transforms into the $KMnF_4{\cdot}H_2O$ monohydrate structure when the K_2MnF_6 powder is dissolved in a heated 40% HF solution, with a greater conversion at higher temperatures. A comparison of the crystallographic structure of K_2MnF_6 with the structure of $KMnF_4{\cdot}H_2O$, shown at the bottom of Fig. 8, reveals that half of the Mn complexes have been attacked by water molecules in the hydrate. These complexes lost two fluorine ligands, which are now replaced by water molecules. One ultimately ends up with one incorporated water molecule per Mn atom. The formation of

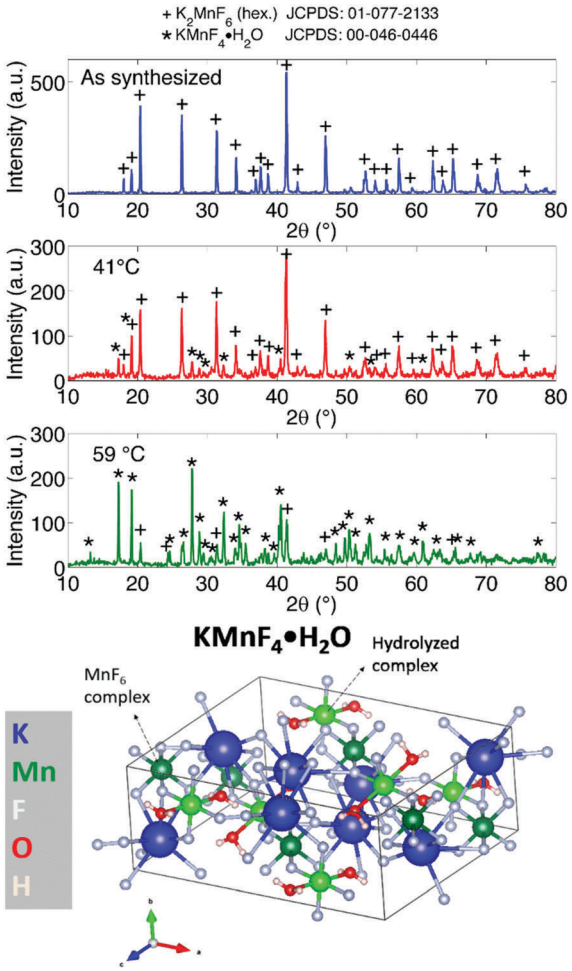

Fig. 8 (top) XRD pattern of dried precipitates produced by heating K_2MnF_6 in 40% HF solutions to set temperatures and the addition of acetone as a nonsolvent. (bottom) Structure of $KMnF_4{\cdot}H_2O$. Some MnF_6 complexes have two fluorine atoms substituted by H_2O molecules. Dark green atoms are manganese atoms in MnF_6 complexes. The light green Mn atoms are the centres of the hydrolysed complexes.

these metal aqua-complexes in K_2MnF_6 is in accordance with ref. 37, in which hydrolysis reactions were considered to cause parasitic effects on the K_2MnF_6 luminescence. Hydrolysis and hydration could replace fluorine ions with water molecules, potentially forming oxygen octahedrons during K_2MnF_6 synthesis. These MnO_6 octahedrons could explain the K_2MnF_6 luminescence above 680 nm observed at 75 K. As shown in Fig. 9, this emission is similar to the one found in Mn(IV) doped oxides where Mn^{4+} is coordinated by an oxygen octahedron. For Mn^{4+} in an octahedral fluorine environment, like in *e.g.* K_2SiF_6:Mn^{4+}, the emission is blue-shifted by about 50 nm.[15] Hydrolysis reactions are thus a major challenge when synthesizing and using K_2MnF_6 during fluoride phosphor synthesis. As with the H_2O_2 addition rate in K_2MnF_6 synthesis, the addition rate of the KF/K_2MnF_6/HF solution during the fluoride phosphor synthesis should also be fine-tuned to minimize these hydrolysis reactions that irreversibly reduce Mn^{4+} to Mn^{3+} and lead to hydrated structures. To verify whether the crystal water in $KMnF_4{\cdot}H_2O$ could be evaporated,

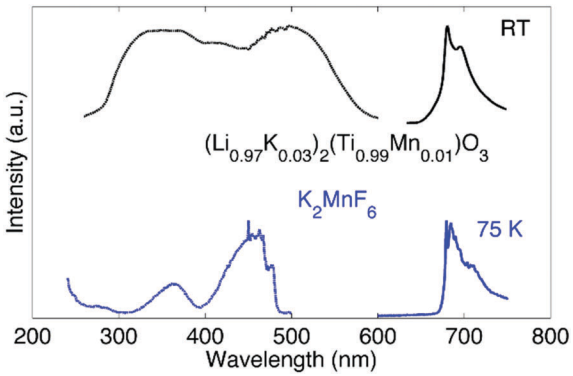

Fig. 9 Luminescence emission (solid line) and excitation (dotted line) spectra of $(Li_{0.97}K_{0.03})_2(Ti_{0.99}Mn_{0.01})O_3$ at RT (top, taken from ref. 38) and K_2MnF_6 at 75 K (bottom).

$KMnF_4{\cdot}H_2O$ was heated in N_2 up to 600 °C and followed using *in situ* XRD (Fig. 10). As can be seen, if the temperature is increased above 145 °C, the crystal water is evaporated from the hydrate, leaving $KMnF_4$ behind. $KMnF_4$ decomposes upon further heating into $KMnF_3$ with the loss of fluorine, probably through HF liberation. As will be cleared out in the following section, the reduction of Mn^{4+} can cause parasitic optical absorption and might lower the efficiency of the final fluoride phosphor synthesized using the impure or degraded K_2MnF_6 precursor.

Diffuse reflectance and X-ray absorption of K_2MnF_6

The influence of Mn^{3+} formation on the optical absorption behaviour of K_2MnF_6 was investigated by diffuse reflectance measurements on MnF_2, MnF_3, ($KMnF_4{\cdot}H_2O$/K_2MnF_6), K_2MnF_6, (K_2MnF_6/$K_2MnF_5{\cdot}H_2O$/KHF_2) and aged K_2MnF_6. The parentheses indicate that the powder was a combination of multiple crystalline phases as was verified by XRD. For the aged sample, conditions of 60 °C and 50% RH were used. The complete diffuse reflectance spectra of the compounds are shown in Fig. 11a. Fig. 11b shows a more detailed part of the reflection patterns in the areas of interest. In MnF_2, used as a Mn^{2+} reference here, a smooth broad absorption band is seen which increases on going from larger to

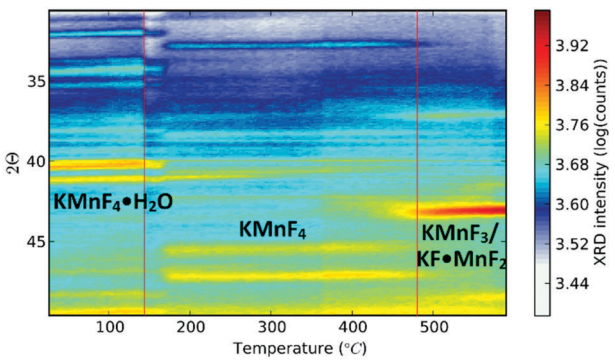

Fig. 10 *In situ* XRD measurement performed on the $KMnF_4{\cdot}H_2O$ monohydrate structure. As the temperature is increased water evaporates from the hydrate, leaving dehydrated $KMnF_4$. Further heating produces the $KMnF_3$ crystalline phase.

smaller wavelengths. No sharp absorption features can be observed. On the other hand, clear signatures of Mn^{3+} are found in MnF_3 (used as a Mn^{3+} reference). Two sharp minima are visible at 432 nm and 518 nm together with a broader absorption band around 800 nm, indicated by the arrow in Fig. 11a.

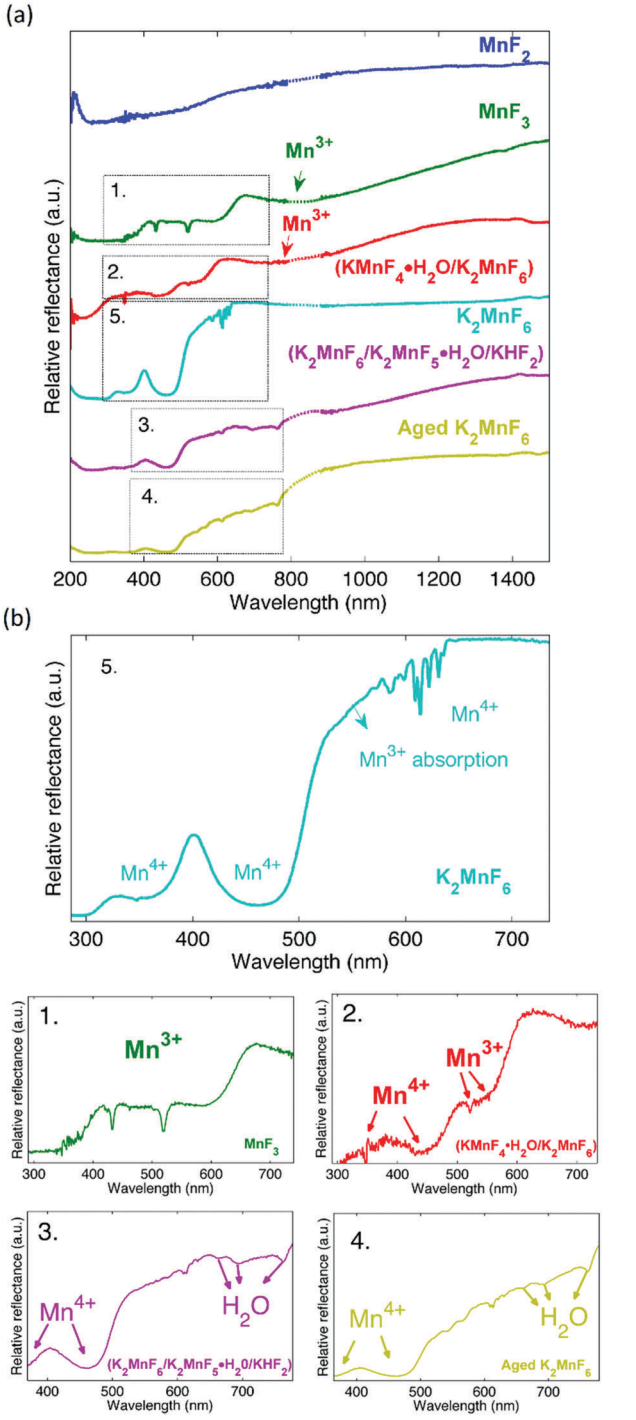

Fig. 11 (a) Diffuse reflectance measurement on diverse fluorides. The interpolated data in the region where the detector is switched are indicated by a dashed line. The spectra are displaced vertically for clarity. (b) Enlarged areas of the diffuse reflectance spectra in figure (a).

Furthermore, a drop in the diffuse reflectance is observed below 664 nm and below 413 nm, forming a staircase like feature in the reflectance spectrum. As expected, a similar behaviour is seen in ($KMnF_4 \cdot H_2O/K_2MnF_6$). This confirms the presence of Mn^{3+} in the hydrated compound. A comparison of the diffuse reflectance spectrum of ($KMnF_4 \cdot H_2O/K_2MnF_6$) with the diffuse reflectance of pure K_2MnF_6 reveals that Mn^{4+} absorption bands around 350 nm and 450 nm are also present. These absorption bands can be assigned to the $^4A_{2g} \rightarrow {}^4T_{1g}$ and $^4A_{2g} \rightarrow {}^4T_{2g}$ electronic transitions in Mn^{4+}, respectively.[39] In the case of ($K_2MnF_6/K_2MnF_5 \cdot H_2O/KHF_2$), the part of the broad Mn^{3+} absorption band above 800 nm can still be observed. However, below 800 nm the diffuse reflectance shows a different behaviour than was the case in the previously described Mn^{3+} containing compounds. If compared with the diffuse reflectance measurement on the aged K_2MnF_6, a similar behaviour is observed. Likely, absorbed water in the aged K_2MnF_6 and $K_2MnF_5 \cdot H_2O$ influences the optical absorption behaviour below 800 nm of both compounds. To conclude, indications exist that even purified K_2MnF_6, without traces of parasitic crystalline phases in XRD, can still contain a considerable fraction of Mn^{3+} ions. The 450 nm absorption band corresponding to Mn^{4+} in K_2MnF_6 is accompanied by an extra absorption band on the longer wavelength side, which is superposed on the sharp Mn^{4+} absorption lines around 620 nm. A comparison with the MnF_3 and ($KMnF_4 \cdot H_2O/K_2MnF_6$) spectra suggests that this broad absorption might be due to a fraction of the Mn ions that are in the 3+ valence state. To verify this, XANES measurements on Mn foil, MnF_2, MnF_3 and K_2MnF_6 were performed. The XANES results are shown at the top of Fig. 12. Here, it is clear that the absorption edge energies shift towards higher energy values as the oxidation state of Mn is increased from 0 (Mn foil) towards 4+ (K_2MnF_6). To determine the edge position of each compound more accurately, the first derivative spectra, shown in the middle of Fig. 12, are used. In the case of MnF_2, MnF_3 and K_2MnF_6, the global maximum is taken as the K-edge position for the octahedral fluorine coordination of Mn^{2+}, Mn^{3+} and Mn^{4+}, respectively. However in the case of pure Mn foil the first maximum is taken as the edge position for neutral Mn. The reason behind this will be explained later on. If the absorption edge energy is plotted against the assumed dominant Mn valence in MnF_2, MnF_3 and K_2MnF_6, all having similar octahedral fluorine coordination of Mn, a linear relationship is obtained. This confirms the dominant contribution of Mn^{2+}, Mn^{3+} and Mn^{4+} in MnF_2, MnF_3 and K_2MnF_6, respectively. However, as Mn is vulnerable to valence changes, multivalence of the Mn ions in the fluoride powders is probable. Partial reduction and oxidation of the Mn within the fluoride powders indeed contributes to the XANES spectra. As can be seen in the MnF_2 derivative curve, small contributions of neutral and trivalent Mn can be found as relative maxima at the edge positions of neutral and trivalent Mn. Likewise, the MnF_3 first derivative curve shows relative maxima at the edge energies of neutral and tetravalent manganese, again indicating partial reduction and oxidation of the Mn ions in MnF_3. In the Mn foil, we ascribe the additional peaks at higher energies in the

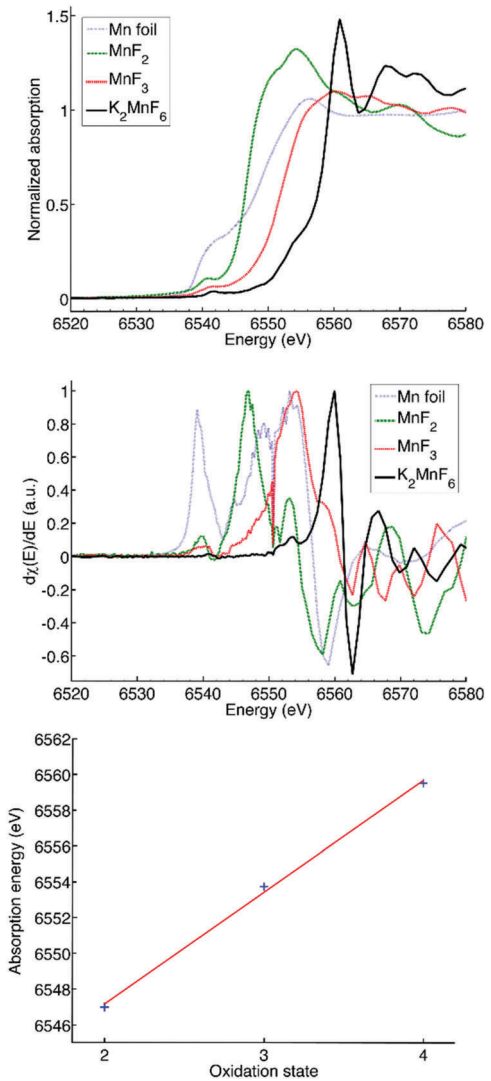

Fig. 12 Top: XANES measurement on Mn foil, MnF_2, MnF_3 and K_2MnF_6. Middle: First derivative spectra of the curves in the top figure. Bottom: Linear fit of the absorption edge energy as a function of the Mn oxidation state.

first derivative spectrum to oxidized Mn. Probably contact with air caused the (surface) formation of diverse manganese oxides. In K_2MnF_6, a second smaller maximum is found in the derivative spectrum which moreover coincides with the global Mn^{3+} maximum. Hence it is likely that a fraction of the Mn ions in K_2MnF_6 is in a 3+ valence state rather than the desired 4+. Since no traces were found in XRD, this indicates that the reduction of Mn^{4+} to Mn^{3+} does not always involve crystalline phase formation.

Based on a Gaussian peak fit of the Mn^{3+} and Mn^{4+} derivative XANES spectra, the fraction of trivalent manganese ions in K_2MnF_6 can be estimated to be smaller than 20%. Remarkably, no clear indications of neutral Mn and Mn^{2+} were found, confirming that the initial synthesis related hydrolysis processes predominantly lead to the formation of Mn^{3+}. Mn^{2+} on the other hand is formed by hydrolysis in air at higher temperatures as was shown in the section concerning the structural properties of K_2MnF_6.

Conclusions

K_2MnF_6 is an essential precursor in the two-step co-precipitation synthesis of Mn^{4+} doped red-emitting fluoride phosphors. K_2MnF_6 incorporates Mn^{4+} in a fluorine octahedron, thereby stabilizing the 4+ valence state of Mn, as required. Nevertheless, the purity of K_2MnF_6 is an issue as both synthesis and degradation by hydrolysis and heat produce several impurities. This can in turn cause defects and impurities in the final phosphor, thereby worsening thermal quenching and lowering the phosphor efficiency. Firstly, the synthesis of K_2MnF_6 is impeded by the formation of KHF_2, a highly corrosive salt which melts at 239 °C. It is caused by the interaction of KF with HF in the synthesis solution. KHF_2 should be washed out by an additional washing step in HF before drying the precipitate. A second synthesis related problem arises with insufficient control of the Mn reduction in the synthesis solution. Any excess of H_2O_2 can lead to excessive reduction of Mn, often leading to hydrated structures such as $K_2MnF_5{\cdot}H_2O$. Furthermore, diffuse reflectance, XAS and XRD showed that the presence of Mn^{3+} does not *a priori* lead to crystalline impurity phases such as a hydrate structure. Even when a pure K_2MnF_6 powder is obtained, further synthesis steps may cause a valence change of the Mn^{4+} ions. Hydration and hydrolysis can take place when K_2MnF_6 is dissolved in heated HF solutions which are used in phosphor synthesis. $KMnF_4{\cdot}H_2O$ was found in XRD measurements as an impurity after dissolving K_2MnF_6 in 40% HF at elevated temperatures. The pristine $[MnF_6]^{2-}$ complexes in K_2MnF_6 have been hydrolysed, resulting in water molecules which take the place of fluorine. In this way, $KMnF_4{\cdot}H_2O$ is formed. Moreover, Mn^{4+} reduces to Mn^{3+}, the latter affecting the optical properties of the final phosphor materials. Apart from synthesis difficulties, care should also be taken in the storage of K_2MnF_6. The hygroscopic nature of K_2MnF_6 shows that this compound is easily hydrolysed by water vapour in air, as could be seen by the large difference when air or N_2 is used as an annealing atmosphere. Likely, hydrolysis facilitates Mn^{4+} to Mn^{2+} reduction when the temperature is increased. The final 2+ valence state was detected in XRD as $KMnF_3/KF{\cdot}MnF_2$ is formed at temperatures above 300 °C. Therefore, we consider hydrolysis reactions as the main factor impeding the structural stability of K_2MnF_6. The hygroscopic nature of K_2MnF_6 in air and the tendency to form hydrated structures in solutions can severely influence the powder purity during use in the lab.

Conflicts of interest

There are no conflicts of interest to declare.

Acknowledgements

RV, HFS, KK, DP and PFS thank the agency for Innovation by Science and Technology (IWT) for a SBO-IWT grant (SBO130030). Our gratitude also goes out to the staff and infrastructure at the DUBBLE beamline, ESRF, Grenoble, France (proposal 26-01-1110).

References

1 S. Ye, F. Xiao, Y. X. Pan, Y. Y. Ma and Q. Y. Zhang, *Mater. Sci. Eng., R*, 2010, **71**, 1–34.
2 N. Narendran, Y. Gu, J. P. Freyssinier, H. Yu and L. Deng, *J. Cryst. Grow.*, 2004, **268**, 449–456.
3 G. Q. Zhang, W. Dirk van Driel and M. Yazdan Mehr, *Engineering*, 2015, **1**, 170–178.
4 P. F. Smet, A. B. Parmentier and D. Poelman, *J. Electrochem. Soc.*, 2011, **158**, R37–R54.
5 A. Piquette, W. Bergbauer, B. Galler and K. C. Mishra, *ECS J. Solid State Sci. Technol.*, 2015, **5**, R3146–R3159.
6 Q. Zhou, H. Y. Tan, Y. Y. Zhou, Q. H. Zhang, Z. L. Wang, J. Yan and M. M. Wu, *J. Mater. Chem. C*, 2016, **4**, 7443–7448.
7 International Telecommunication Union, 2012.
8 J. H. Oh, Y. J. Eo, H. C. Yoon, Y. D. Huh and Y. R. Do, *J. Mater. Chem. C*, 2016, **4**, 8326–8348.
9 Y. H. Kim, P. Arunkumar, B. Y. Kim, S. Unithrattil, E. Kim, S.-H. Moon, J. Y. Hyun, K. H. Kim, D. Lee, J.-S. Lee and W. B. Im, *Nat. Mater.*, 2017, **16**, 543–550.
10 Y. Hu, W. Zhuang, H. Ye, S. Zhang, Y. Fang and X. Huang, *J. Lumin.*, 2005, **111**, 139–145.
11 X. Piao, K. Machida, T. Horikawa, H. Hanzawa, Y. Shimomura and N. Kijima, *Chem. Mater.*, 2007, **19**, 4592–4599.
12 Y. Q. Li, J. E. J. van Steen, J. W. H. van Krevel, G. Botty, A. C. A. Delsing, F. J. DiSalvo, G. de With and H. T. Hintzen, *J. Alloys Compd.*, 2006, **417**, 273–279.
13 Z. Zhou, N. Zhou, M. Xia, M. Yokoyama and H. T. Hintzen, *J. Mater. Chem. C*, 2016, **4**, 9143–9161.
14 H. F. Sijbom, J. J. Joos, L. I. D. J. Martin, K. Van den Eeckhout, D. Poelman and P. F. Smet, *ECS J. Solid State Sci. Technol.*, 2016, **5**, R3040–R3048.
15 H. F. Sijbom, R. Verstraete, J. J. Joos, D. Poelman and P. F. Smet, *Opt. Mater. Express*, 2017, **7**, 3332–3365.
16 X. Y. Jiang, Y. X. Pan, S. M. Huang, X. Chen, J. G. Wang and G. K. Liu, *J. Mater. Chem. C*, 2014, **2**, 2301–2306.
17 S. Adachi, H. Abe, R. Kasa and T. Arai, *J. Electrochem. Soc.*, 2012, **159**, J34–J37.
18 M. Du, F. Tang, J. Long, C. Ma, X. Yuan, J. Zhang, Z. Wen, R. Ma and Y. Cao, *Mater. Res. Bull.*, 2016, **83**, 316–323.
19 H. Zhu, C. C. Lin, W. Luo, S. Shu, Z. Liu, Y. Liu, J. Kong, E. Ma, Y. Cao, R. S. Liu and X. Chen, *Nat. Commun.*, 2014, **5**, 4312.
20 Q. Zhou, Y. Y. Zhou, Y. Liu, Z. L. Wang, G. Chen, J. H. Peng, J. Yan and M. M. Wu, *J. Mater. Chem. C*, 2015, **3**, 9615–9619.
21 S. Adachi and T. Takahashi, *J. Appl. Phys.*, 2009, **106**, 013516.
22 Y. K. Xu and S. Adachi, *J. Appl. Phys.*, 2009, **105**, 013525.
23 Q. Zhou, Y. Y. Zhou, Y. Liu, L. J. Luo, Z. L. Wang, J. H. Peng, J. Yan and M. M. Wu, *J. Mater. Chem. C*, 2015, **3**, 3055–3059.
24 S. Adachi and T. Takahashi, *J. Appl. Phys.*, 2008, **104**, 023512.
25 L. Lv, X. Jiang, S. Huang, X. A. Chen and Y. Pan, *J. Mater. Chem. C*, 2014, **2**, 3879.
26 B.-E. Yeo, Y.-S. Cho and Y.-D. Huh, *Opt. Mater.*, 2016, **51**, 50–55.
27 D. H. Kim, J. Ju and D. Y. Jeong, *New Physics: Sae Mulli*, 2016, **66**, 311–316.
28 A. A. Setlur, E. V. Radkov, C. S. Henderson, J.-H. Her, A. M. Srivastava, N. Karkada, M. S. Kishore, N. P. Kumar, D. Aesram, A. Deshpande, B. Kolodin, L. S. Grigorov and U. Happek, *Chem. Mater.*, 2010, **22**, 4076–4082.
29 T. T. Deng, E. H. Song, J. Sun, L. Y. Wang, Y. Deng, S. Ye, J. Wang and Q. Y. Zhang, *J. Mater. Chem. C*, 2017, **5**, 2910–2918.
30 L.-L. Wei, C. C. Lin, M.-H. Fang, M. G. Brik, S.-F. Hu, H. Jiao and R.-S. Liu, *J. Mater. Chem. C*, 2015, **3**, 1655–1660.
31 F. Tang, Z. Su, H. Ye, M. Wang, X. Lan, D. L. Phillips, Y. Cao and S. Xu, *J. Mater. Chem. C*, 2016, **4**, 9561–9568.
32 H. J. H. Bode and F. Bandte, *Angew. Chem.*, 1953, 304.
33 P. F. Smet and J. J. Joos, *Nat. Mater.*, 2017, **16**, 500–501.
34 A. P. Giddy, M. T. Dove, G. S. Pawley and V. Heine, *Acta Crystallogr., Sect. A: Found. Crystallogr.*, 1993, **49**, 697–703.
35 M. T. Dove, *Am. Mineral.*, 1997, **82**, 213–244.
36 R. Kasa, Y. Arai, T. Takahashi and S. Adachi, *J. Appl. Phys.*, 2010, **108**, 113503.
37 A. M. Black and C. D. Flint, *J. Chem. Soc., Dalton Trans.*, 1974, **15**, 977–981.
38 S. K. K. Seki, K. Uematsu, T. Ishigaki, K. Toda and M. Sato, *Journal of Ceramic Processing Research*, 2013, **14**, s67–s70.
39 R. Kasa and S. Adachi, *J. Electrochem. Soc.*, 2012, **159**, J89–J95.